LuBan: Low-Cost and In-Situ Droplet Micro-Sensing for Inkjet 3D Printing Quality Assurance

Aosen Wang*   Tianjiao Wang*   Chi Zhou   Wenyao Xu

University at Buffalo, the State University of New York, NY, 14260, USA

{aosenwan,twang38,chizhou,wenyaoxu}@buffalo.edu

ABSTRACT

Inkjet 3D printing is a disruptive manufacturing technology in emerging metal- and bio-printing applications. The nozzle of the printer deposits tiny liquid droplets, which are subsequently solidified on a target location. Due to the elegant concept of micro-droplet deposition, inkjet 3D printing is capable of achieving a sub-millimeter scale manufacturing resolution. However, the droplet deposition process is dynamic and uncertain which imposes a significant challenge on *quality assurance* of inkjet 3D printing in terms of product reproducibility and process repeatability. To this end, we present Luban as a certification tool to examine the printing quality in the inkjet printing process. Luban is a new *low-cost* and *in-situ* droplet micro-sensing system that can precisely detect, analyze and localize a droplet. Specifically, we present a novel tiny object sensing method by exploiting the computational light beam field and its sensitive interference effect. The realization of Luban is associated with two technical thrusts. First, we study integral sensing, i.e., a new scheme towards computational light beam field sensing, to efficiently extract droplet location information. This sensing scheme offers a new *in-situ* droplet sensing modality, which can promote the information acquisition efficiency and reduce the sensing cost compared to prior approaches. Second, we characterize interference effect of the computational light beam field and develop an efficient integration-domain droplet location estimation algorithm. We design and implement Luban in a real inkjet 3D printing system with commercially off-the-shelf devices, which costs less than a hundred dollars. Experimental results in both simulation and real-world evaluation show that Luban can reach the certification precision of a sub-millimeter scale with a 99% detection accuracy of defect droplets; furthermore, the enabled *in-situ* certification throughput is as high as over 700 droplets per second. Therefore, the performance of our Luban system can meet the quality assurance requirements (e.g., cost-effective, *in-situ*, high-accuracy and high-throughput) in general industrial applications.

CCS CONCEPTS

• **Computer systems organization** → **Embedded and cyber-physical systems**; *Sensors and actuators*; Embedded hardware;

KEYWORDS

3D Printing; Light Beam Sensors; Experimentation.

1 INTRODUCTION

Inkjet 3D printing [28] is one of the most popular printing techniques in rapid prototyping and additive manufacturing to produce the object from a digital model. The inkjet 3D printing process deposits a sequence of micro-scale (sub-millimeter) liquid droplets and thus can achieve higher resolution and accuracy compared to other competing 3D printing technologies such as Fuse Deposition Modeling (FDM) [39], Stereolithography (SLA) [47] and Selective Laser Sintering (SLS) [38]). The variation of droplet material can even enable innovative printing applications, such as metal printing (e.g., aerospace and automobile components [19, 22]) and bio-printing (e.g., soft tissues [9] and live organs [17]).

The key unsolved problem of inkjet 3D printing technology in real-world applications is the lack of robust methods and inspection techniques to qualify and certify the part reproducibility and process repeatability, due to the following two reasons. 1) High Precision Requirement: Considering that the inkjet 3D printing technology aims at high-dependable military and biomedical applications, the quality assurance of products must meet the sub-millimeter level droplet sensing precision [11]. A millimeter-level drift in process conditions will drastically impair build quality in inkjet 3D printing. The inspection tool with higher precision than the process resolution is highly desirable but unfortunately challenging due to the complicated dynamic jetting process. 2) High Throughput Requirement: In order to obtain the trustworthy quality assurance, the dependable approach is to *in-situ* verify the process quality because the post-product examination [15] cannot effectively obtain inside geometric and quality information. Therefore, the in-process as opposed to post-process verification needs to be high-throughput without compromising the machine productivity. We have exhaustively examined the available sensing solutions, and they cannot meet either the precision requirement (e.g., ultrasound [8], infrared [26] and RF [29]) nor high throughput requirement (e.g., high-resolution camera [24]). Advanced light and electron microscope techniques [13] have potential to reach the design goal, however, it hinders the practicality due to the fact that an ultra-fast microscope machine costs from hundreds of thousand to millions of dollars.

To enable practical quality assurance in inkjet 3D printing, we argue that the product certification tool should be able to monitor the droplet precision on the fly. To this extent, we present the first *in-situ* droplet micro-sensing system, named LuBan[1], as a certification tool to evaluate the in-process quality of inkjet 3D printing. To accurately and reliably sense the behavior of droplets, we employ low-cost infrared diode to implement high precision (sub-millimeter level) sensing with the help of the computational light beam field. By analyzing the characteristics of the light beam field, we clarify the practical challenges to design LuBan, i.e., computational light beam field sensing and integration-domain droplet localization algorithm. Specifically, we propose to apply an integral sensing model into computational light beam field sensing for dimension reduction while keeping the salient location information. We also thoroughly design the physical sensing modality to implement the data integral process. Moreover, we develop an integration-domain droplet location algorithm, which specifically works on the integral field representation, by jointly applying analytical geometry and optimization methods to improve the precision and robustness of droplet behavior sensing. For a comprehensive evaluation, we conduct the complementary simulated study and real-world study to examine the performance of LuBan and impacts to the entire inkjet 3D printing system. The results indicate that our LuBan system can achieve sub-millimeter sensing accuracy, around 100 microns, with more than 99% recognition rate of defect droplet location and 725 droplets-per-second throughput. To our best knowledge, LuBan is the first droplet micro-sensing system which is designed to examine the in-process quality of inkjet 3D printing.

Our contribution can be summarized as three-fold:

- We open up a new angle to address the 3D printing quality assurance issue by micro-sensing droplet behavior. Most existing efforts focus on parameter tuning of droplet generation.
- We prove the feasibility of utilizing the computational light beam field to design our droplet micro-sensing system, LuBan. For the sake of sensing efficiency and system costs, we explore a new integral sensing modality based on computational light beam field and associated integration-domain data processing.
- We design a complementary simulation study and real-world study to validate the performance of our Luban system. The simulation study profiles the Luban's system characterization and the real-world study verifies the Luban's effectiveness in 3D printing setups.

Besides precision improvement for quality assurance, the Luban droplet micro-sensing system has three more advantages: (1) The entire system is cost-effective. The low-cost infrared diode is a mature product and widely used in industry. LuBan is *in-situ* correction enabled. Compared with offline monitoring, our LuBan can provide accurate and instant droplet state information, which is critical to precise and reliable quality assurance. (2) LuBan has good accessibility which is easy to be deployed into other existing 3D printing systems [6]. (3) The sensing information of our LuBan

is a low-dimension integral signal, which is helpful to reduce the risk [40] of information disclosure.

The remainder of this paper is organized as followings: Section 2 introduces the basic principles and preliminaries of inkjet 3D printing. The concept and practical challenges of light beam field are presented in Section 3. Section 4 describes the system overview of our droplet micro-sensing design. The computational light beam field sensing in LuBan system is investigated in Section 5, and the integration-domain droplet location algorithm is elaborated on in Section 6. Section 7 discusses our motivation and methodology of the evaluation plan for Luban System. In Section 8, the simulated study is conducted and the real-world study is carried out in Section 9. Section 10 includes the related work. Finally, we conclude our work in Section 11.

2 BACKGROUNDS

In this section, we provide a brief introduction to the basics of inkjet 3D printers. We also discuss the significance of precision for droplet sensing system in inkjet 3D printing quality assurance application.

2.1 Inkjet 3D Printers

Inkjet 3D printing is an additive manufacturing process that works in a similar way as the inkjet 2D printing used on a daily basis. The liquid material is jetted out from the nozzle (print head) as a sequence of micro-droplets and then solidified on the partially printed part. While the print head moves over the printing area based on the digital model, the jetted material is added and bound with the previous layer. The platform elevates downward by one layer-thickness after the current layer is formed. By repeating this process, the part is constructed in a layer-by-layer fashion. Fundamentally, the inkjet 3D printing process converts the liquid material into solid and the solidification mechanism includes cooling molten material, freezing naturally liquid material, the evaporation of an aqueous solution, gluing loose power, photo/thermal-polymerizing thermoset materials, a chemical reaction induced covalent bonding etc.
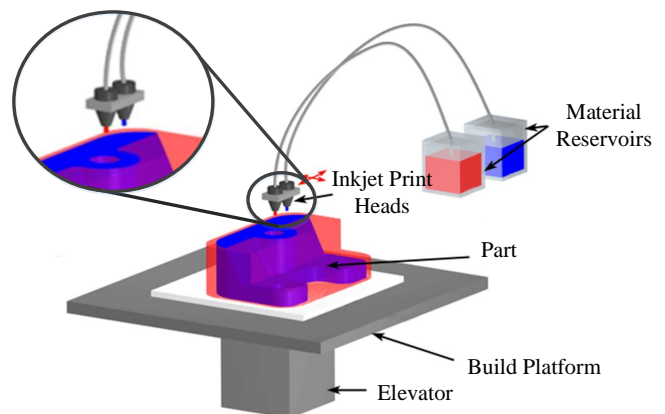

Figure 1: The inkjet 3D printer structure.

A typical inkjet 3D printer is shown in Figure 1. A nozzle or a print head is used to generate micro-size droplets of the printed

---

[1]LuBan is a typical representative of the sophisticated-skilled artisan in Chinese tale [1].

material. The droplet is jetted to the solidified part and the liquid material is continuously fed into the print head during the printing process. A motion system, usually the linear stages, is necessary to accurately move the print head to desired locations, which is controlled by a microcontroller based on the geometry of the printing part.

2.2 Significance of Quality Assurance

Inkjet 3D printing is a promising advanced manufacturing technology. Quality assurance is to examine key parameters in the manufacturing process to certify 3D printed products. Specifically, process precision, i.e., the droplet location, is the key quality metric which can facilitate the broader applications of inkjet 3D printers. Three representative implications of precision are summarized as follows:

Printing quality: First of all, the precision leads to improved printing quality, which includes geometry integrity and functional integrity. The printing quality is the key that limits the application of inkjet 3D printing.

Environment adaptivity: Inkjet 3D printing is desired to be environmentally friendly to expand its widespread applications. Better precision can avoid the unfavorable environmental conditions, such as vibration which will negatively affect the inkjet 3D printing process.

Resource economization: Inkjet 3D printing is a one-time process, that is if there is any defect generated, the entire part must be abandoned and built again. This will result in energy and resource waste, violating the concept of current green manufacturing paradigms. The precision can enable more energy and resource savings.

3 LIGHT BEAM FIELD: CONCEPT AND CHALLENGES

The light beam field is an innovative approach to accurately sense the droplet to enable quality assurance in inkjet 3D printing. In this section, we introduce the concept and characteristics of light beam field. We investigate the field interference effect, which is promising to locate the tiny object in light beam field. Eventually, we summarize the practical challenges to design a droplet micro-sensing system based on field interference.

3.1 Concept

Light beam field is a characterized energy field distribution which results from a light source dispersing energy through the electromagnetic wave. The infrared diode is a prevalent emitter [34], which is reliable and widely applied in industrial practice. The concept of light beam field from the infrared diode is shown in Figure 2. The infrared light is generated when an electric field is applied to a P-N junction in the diode. The electrons are pushed from the N-region and recombine with the holes in the P-region. To lessen the energy level, extra energy is emitted in the form of heat and light. From the generation and principle of light beam field, we can observe three characteristics:

- **Field Repeatability:** The light beam field is stable and repeatable. Its distribution is dependent on the optical structure
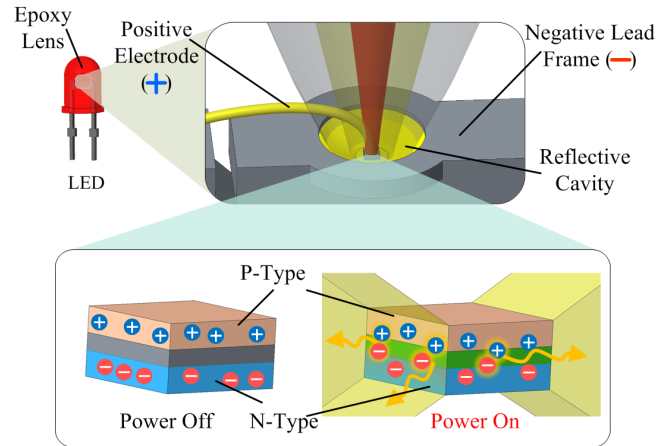

Figure 2: The concept of light beam field generation, which conveys three characteristics, field repeatability, energy continuity and energy anisotropy.

including epoxy lens/case, electrode structure and reflective cavity shape on the lead frame [31]. These mechanical structures are stable during the whole lifetime of the light-emitting diode (LED), which provides us the basis to model the field.

- **Energy Continuity:** In a stable light beam field, the LED has a high effectiveness of more than 70% [32]. In a 250 mW LED, more than 10^{20} photons of 950nm wavelength are generated in a second [2]. All the energy is distributed in a small area of 10 mm^2 that makes it continuous along any direction.

- **Energy Anisotropy:** The energy anisotropy [5] indicates that the energy is not uniformly distributed, caused by the effect of the reflective cavity and the refraction of the epoxy lens/case. The radiant energy density [46] is much higher at the point closer to the center axis and closer to the LED. Due to the energy anisotropy, an interference happening at different locations will have different intensity of impact in the beam field. This provides good sensitivity to estimate the location of a tiny object in the field.

3.2 Field Interference Effect

Field interference effect utilizes the electromagnetic disturbance to sense the tiny intruder object. When a small piece enters the light beam field, the interactions between object and field, including absorbing, reflection, diffraction and refraction, will change the original energy density distribution. This phenomenon is called "field interference" [35]. By measuring this interference effect, according to the intrinsic energy anisotropy, it is possible to accurately infer the state of an intruder when interaction happens.

We provide an example of interference effect, when a droplet passes through the light beam field, in Figure 3. The light beam field is built by a typical infrared emitter, as shown in Figure 3(a). The field intensity is distributed stably and continuously. If the droplet
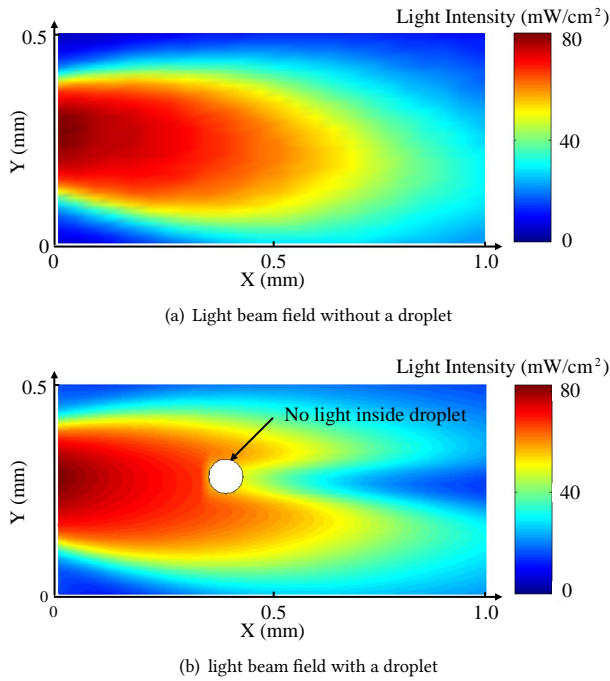
(a) Light beam field without a droplet

(b) light beam field with a droplet

Figure 3: An example of light beam field with and without interference from the droplet.

enters into the field, as shown in Figure 3(b), we can observe obvious field intensity changes. The droplet induces an irregular and complex intensity pattern. By quantitatively sensing this interference effect, it is promising to estimate the location of a tiny object in the field. However, we can also find that the droplet not only affects the field distribution at its own location, but also its surrounding area along the light emitter direction.

3.3 Practical Challenges

In inkjet 3D printing applications, the droplet location is the key factor affecting the printing quality. Light beam field is promising to be applied to the task of droplet location sensing to improve printing precision. Towards a practical system design, two urgent challenges, i.e., light beam field sensing and droplet location algorithm, need to be addressed.

Light Beam Field Sensing: Although we can observe obvious interference effect between the beam field and the droplet, it is still a challenge to efficiently sense the interference. Due to the complex field patterns and the motion of droplets, brute-forcingly detecting radiant intensity at each location in the beam field to represent the field energy distribution is obviously unfeasible. A sensing paradigm with a larger information density is highly favored.

Droplet Location Algorithm: We need to investigate how to accurately and efficiently estimate the droplet position from sensing data. Considering the characteristics of sensor design and practical non-ideal deployment, the location algorithm needs to be carefully

designed to recover the droplet location information from noisy data inputs with the precision and real-time constraints.

4 LUBAN: IN-SITU DROPLET MICRO-SENSING SYSTEM

In this section, we introduce the design of our *in-situ* droplet micro-sensing system for the precision 3D printer. We mainly tackle the two practical challenges mentioned in Section 3.3. Our description starts from the system overview. We also illustrate the role of each module in the system.

4.1 System Overview

The droplet precision is the critical factor in printing quality and reliability of inkjet 3D printer. Our LuBan system aims to precisely and efficiently sense the location of droplets in order to qualify and certify the repeatability of the printing process. We provide the system overview of our Luban in Figure 4 in a real inkjet printing task. The entire system comprises two key components, computational light beam field sensing and integration-domain droplet location algorithm. Computational light beam field sensing includes integral sensing model and its hardware implementation. The integration-domain droplet location algorithm consists of key feature extraction, analytical model look-up table, field model indexing and droplet location fine-tuning module. The integral sensing module tends to acquire the light beam field interference pattern and reduce the dimension of the intractable field representation for the ease of practical analysis. The key feature extraction module is designed to find the identification of integration-domain field representation. Based on this identification, the field model indexing module can return the parametric analytical model belonging to a specific key feature. The analytical model look-up table is built from light beam field characterization. Finally, the droplet location fine-tuning module calculates the droplet position from the analytical models.

4.2 Module Details

Integral Sensing Model: When the droplet goes through the light beam field, it will interact with the field, resulting in a high-dimensional complex light energy pattern. However, it is intractable to acquire the exact pattern of this interference in the analog domain. Therefore, dimension reduction is a necessary step to lower the field measuring complexity while keeping the salient information for droplet location. We apply integral sensing to reduce the signal dimension from analog domain to digital domain to make light beam field "computational". It can not only integrate the original complex field into low-dimension digital representation, but also guarantee the information preserving by sensor number selection. A new sensing modality is also designed to implement the integral process on hardware for computational light beam field sensing.

Analytical Model Look-Up Table: Before calculating the droplet location information, we first conduct a preliminary study to build a look-up table of static integral field patterns for a single pair of light sensors. We apply the robust *Gaussian* model to fit the sensing data in the preliminary study. This look-up table will be shared by all the sensor pairs in the sensing modality.
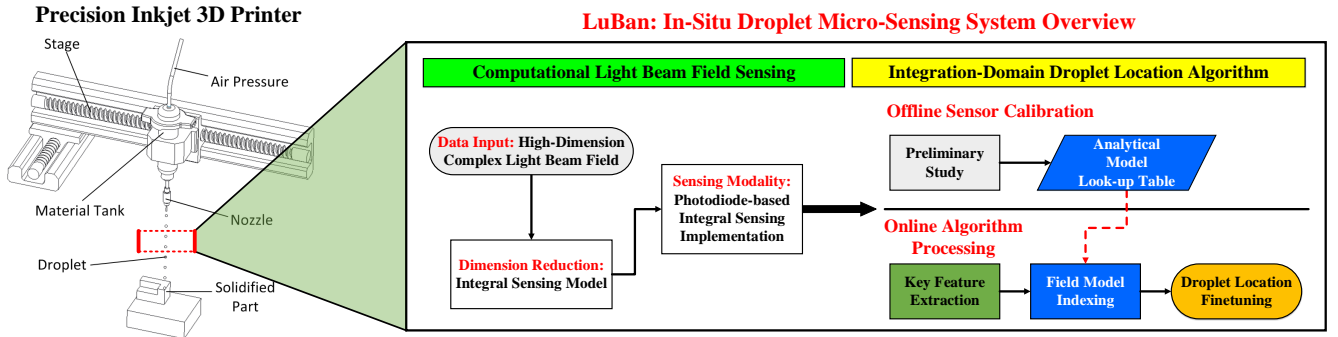
Precision Inkjet 3D Printer

Figure 4: The system overview of *in-situ* droplet micro-sensing for inkjet 3D printing quality assurance.

Key Feature Extraction: The data format obtained from integral sensing model is a time series signal. We propose to extract the key feature of the time series to build the mapping relationship with the analytical model in a look-up table.

Field Model Indexing: Our light beam field model uses a series of parameters of *Gaussian* function to store the static field interference pattern. It can achieve efficient memory and runtime complexity. Once we get the key feature, we can fetch its corresponding model for the preparation of location information estimation.

Droplet Location Fine-Tuning: We will find multiple parametric analytical models from the look-up table due to the number of light sensors. To discern the location uncertainties, we designed a geometry-based optimization method to accurately locate the droplet position in the printing space.

5 COMPUTATIONAL LIGHT BEAM FIELD SENSING

In this section, we introduce our strategy, integral sensing, to efficiently sense the light beam field with interference. For the complex field intensity pattern in 3-D space, we integrate the field by low-dimension representation. To keep enough information preserved, we also discuss the integral process implementation of our LuBan system.

5.1 Integral Sensing Model

The interference between light beam field and droplets occupies a time-varying complex field intensity pattern as the droplet passes through the field. It raises enormous difficulties to quantitatively and accurately detect the changes of the field caused by interference. To address this challenge, a data integration process to reduce the continuous high-dimensional field to the discrete low-dimensional data representation is highly favored. However, the main concern in dimension reduction is to preserve salient information. We propose an integral sensing model to address these issues, whose concept is shown in Figure 5.

The photodiode detector [44] integrates the complex field intensity distribution in 3-D space. Its view area is formed by the two boundaries, as shown by the gray planes in Figure 5. The reading D from the detector is the integral form of the complex pattern of
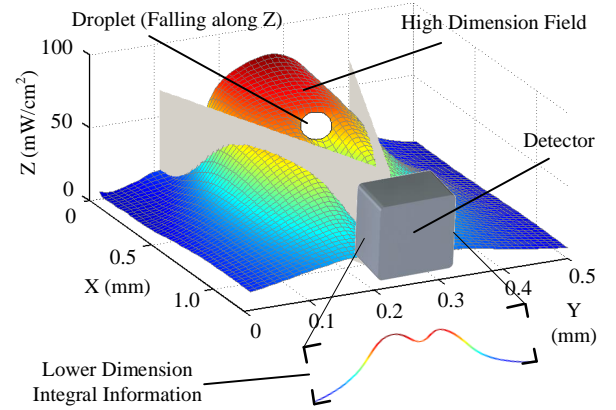

Figure 5: An example of complex field interference pattern sensing by an integral model.

the field F, and the integration process follows the equation:

$$D_{i,p} = \int_a^b \int_{i-\delta t}^i F_{i,p}(t, \phi) \, d_t \, d_\phi, \qquad (1)$$

where $F_{i,p}(t, \phi)$ is the 3-D field intensity at timestamp i and space position p. The parameter d_ϕ integrates the light beam field between the two viewing boundaries, a and b, of the detector. The viewing boundary is decided by the intrinsic property of the photodiode detector. The d_t integrates the light beam field in a short time period δt. It is noted that D_i is a time series because the fourth dimension, time, is considered. Therefore, we call this data dimension reduction method of light beam field as "integral sensing".

The key challenge in field integral sensing is how to keep enough intrinsic information of 2-D droplet position. Reexamination of Eq. (1) shows that one detector can only provide 1-dimensional information from a fixed space position p. It can only sense a partial change of light beam field. An intuitive observation is that one sensor is not enough, because the droplet location is a 2-dimensional information. Therefore, multiple sensors are necessary to collect enough field interference information for droplet location estimation.

We will have two big challenges to develop the hardware sensing part for the integral model, sensor number and sensor layout. For

sensor number, too few sensors are not sufficient to support the accurate droplet location estimation. But too many sensors will bring data redundancy, resulting in increasing computation complexity. The design rule of multiple-sensor layout is to maximize the effective information acquisition for each single sensor.

5.2 Sensing Modality: Integral Sensing Hardware Implementation

In this section, we design the hardware part of LuBan system, a sensor array for sensing field interference. To physically implement the lower dimension process, we use the photodiode detector as a field interference receiver.

5.2.1 Property of Emitter-Detector. In order to make full use of the energy anisotropy of light beam field to achieve a high precision location detection, we illustrate two requirements in the sensor layout design.

Emitter-Detector In-Pair: Energy at multiple locations is required to effectively detect the position of the droplet. However, the light beam field is narrowed down [43] to concentrate the energy for better detection. Due to the narrowed light beam, the single emitter cannot physically cover multiple detectors. Because there is no interference among different light beams during propagation. So we use multiple emitter-detector pairs to detect the energy at different locations.

Emitter-Detector Coplanar: Our aim is to retrieve the location information of a droplet on the solidified part. Thus, all the emitter-detector pairs should be in the same plane which is parallel to the X-Y plane. Its position on the Z axis decides the response time for *in-situ* correction after droplet sensing.

5.2.2 Sensor Layout. Our main task is to identify the number of emitter-detector pairs and the position of each pair. In LuBan system, our final sensor array layout is a three-pair solution with emitter-detector pairs arranged 120 degrees to each other, as shown in Figure 6. We will justify our layout design from information and practical constraints as the following:
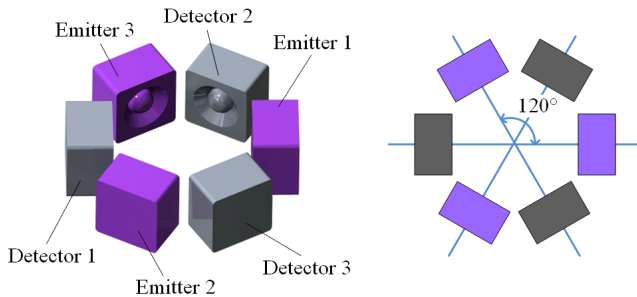

Figure 6: The sensor layout model in LuBan system.

Information Constraints: Due to the information capacity and noise tolerance, the sensor pair number should be no less than three. First, the one-pair solution is obviously not feasible, because the droplet location is a 2-D vector. Although two-pair solution seems qualified to provide enough information, this option is not feasible

either due to its sensitivity to noise. In the system design, noise from the measurement is almost inevitable, which will severely degrade the solution accuracy of the closed-form equations. Our field interference sensing method is to collect multiple local information from light beam field. It functions as an "integral" approach to addressing the dimension issue. Therefore, as discussed in section 5.1, the data dimension can be bounded by three. On the other hand, more than three pairs can indeed provide more information for droplet location estimation with the help of robust optimization algorithms [18]. However, the larger information redundancy also makes the improvement insignificant and in turn increases the algorithm complexity.

Practical Constraints: More than three-pair solutions are extremely difficult to be implemented physically due to the unique small working area of inkjet 3D printing. Specifically, the working area of the printing head of the 3D printer is limited in a 5×5 mm^2 square. However, the size of infrared emitter and receiver is also at the millimeter level.
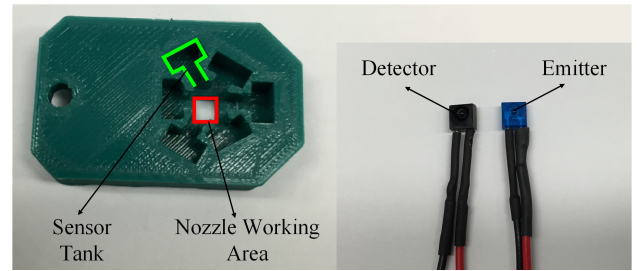

Figure 7: The working area of the printing head and sensor deployment of three pairs.

We provide an example in Figure 7 to show the physical space constraint for a three-pair solution. We can observe that even the three-pair layout needs to be carefully designed and deployed. Additionally, more sensor pairs will also increase the risk of light interference on one detector from different emitters. Therefore, three-pair emitter-receiver is chosen to build the sensor array for our LuBan system. To minimize the light interference risk among the three pairs of emitter and detector, we decide to place them as far as possible with the 120-degree angle between.

6 INTEGRATION-DOMAIN DROPLET LOCATION ALGORITHM

In this section, we introduce the core part of software implementation in LuBan system, droplet location algorithm on integration domain. In this algorithm, the 2-D location information can be estimated from three time series of the sensor array in integration domain. To achieve better accuracy and reliability avoiding noise effect from environmental variables and imperfection of sensor array, we develop our location algorithm based on analytical geometry and optimization techniques. The whole algorithm includes offline sensor calibration and online algorithm processing. The sensor calibration is to obtain the parametric analytical models for computational light beam field. The online algorithm processing includes key feature extraction from integration field representation, field model indexing and droplet location fine-tuning.

6.1 Offline Sensor Calibration

Sensor calibration is required to build the reference in light beam field for the analytical model of the online sensing process. We use a data-driven approach to explore the field intensity change when interference occurs. With the reliable simulation results, we establish the look-up table storing analytical models of *Gaussian* function for the field intensity change, which is a common assumption in similar applications [48]. This model is critical to uncover the intrinsic property of interference effect for the location algorithm design. The final model is recorded by the key parameters of the *Gaussian* function.
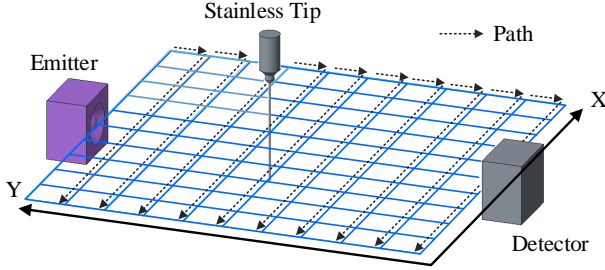

Figure 8: Sensor calibration of light beam field using stainless tip simulation.

Calibration Process: In the calibration process, the characteristic data comes from a simulation of the droplet falling process by a thin stainless tip, as shown in Figure 8. This tip can interfere with the infrared field propagation between the emitter and the detector. The interference effect will cause a stable weakened signal on integration domain output at the detector end. The intensity decreasing the degree of the signal is able to reflect the energy density distribution of the light beam field in this space area. This data-driven simulation can provide us constant output with the stainless tip placed. The output is only related to the infrared beam field distribution and can eliminate impacts from other factors.

Analytical Model Fitting: After we obtain the characteristic data, we choose the analytical model to fit the data distribution for the convenience of data recording and indexing. To this end, we use a group of *Gaussian* functions fitting [16] to model the interference effect on the light beam field in the integration domain, as shown in Figure 9. The single *Gaussian* function is in the X-Z plane and the group of functions is along the Y axis. The format of the *Gaussian* function is expressed as the following:

$$G_Y(X) = h - ae^{-\left(\frac{X-b}{c}\right)^2}|Y, \qquad (2)$$

where h, a, b and c are parameters to describe the *Gaussian* function. The X and Y are the axis components of integration domain measurements and $G_Y(X)$ is the fitted *Gaussian* function on plane Y. If we use all the measurements in plane Y to fit this model, the problem can be formulated as:

$$\{h_0, a_0, b_0, c_0\} = \arg\min_{h,a,b,c} \|Z - G_Y(X)\|_2, \qquad (3)$$

where $\{h_0, a_0, b_0, c_0\}$ is the optimal fitting parameters and Z is the intensity of the integral field. This is a well-studied *Gaussian* fitting problem, which can be solved by off-the-shelf toolbox [21]. For

each plane Y, we execute this fitting process and record the key parameters. After traversing all possible Y plane, we can build the analytical model of characteristic data on the integration domain. We execute this calibration process for the three sensor pairs separately. Note that an exception here is the number of measurements on a certain Y plane is not enough to fit the *Gaussian* function. We will discard such cases.
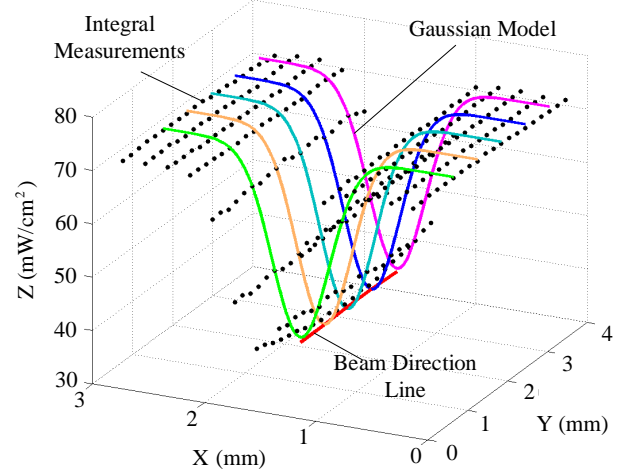

Figure 9: Analytic model fitting for integration domain measurements.

6.2 Online Algorithm Processing

The entire processing for integration domain time series includes three main procedures, key feature extraction, field model indexing and droplet location fine-tuning. We elaborate each part in this section.

6.2.1 Key Feature Extraction. The algorithm starts from time series on the integration domain, obtained from section 5. The peak is a remarkable index feature to fetch the model for the analytical information of the time series. The time series can be denoted as the following:

$$D^i = \{D_1^i, D_2^i, D_3^i...D_n^i\}, \quad where \ i = 1, 2, 3. \qquad (4)$$

The time series data conveys the interference change over time. These integral field representations also have a certain amount of noise, which increases the difficulty of peak detection of time series. We assume each droplet is fully immersed in the light beam field and the size of each droplet is the same which are common cases in practice. Therefore, the trough, or the peak, of the time series data will only relate to the field intensity distribution. Taking efficiency and accuracy into consideration, we adopt an automatic multiscale-based peak detection (AMPD) method [37] to identify the peak (trough) value which is specifically designed for noisy applications. Its formulation is as follows:

$$\sigma_i = \frac{1}{\lambda - 1} \sum_{k=1}^{\lambda} [(m_{k,i} - \frac{1}{\lambda} \sum_{k=1}^{\lambda} m_{k,i})^2]^{\frac{1}{2}}, \qquad (5)$$

where $m_{k,i}$ indicates the matrix value of local maxima scalogram and λ contains the information about the scale-dependent distribution of peaks. The peaks are at index i who holds $\sigma_i = 0$. This method has been proven valid in real world signal peak detection.

6.2.2 Field Model Indexing. The next step of our algorithm processing is to fetch the surface model by the peak value from the time series on the photodiode detectors. Its output is two 3-D space curves which will be used in geometry optimization procedure. With the help of the analytic model, this query can be done by finding the crossing point of the *Gaussian* surface and the plane parallel to the X-Y plane with a height equal to the peak value obtained in the previous key feature extraction, which is illustrated in Figure 10.
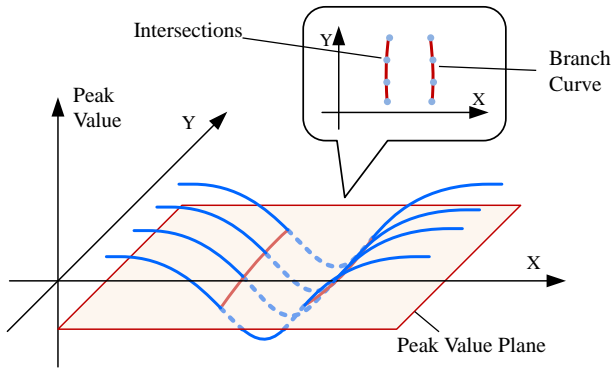

Figure 10: Two branch curves retrieval in field model indexing by peak detection value.

All these candidate points on the intersection curve are the possible locations where the dropping happens. For one pair of the sensor with a single emitter and a single detector, these possible dropping locations form a curve that has two branches.

6.2.3 Droplet Location Fine-Tuning. In this part, we estimate the droplet location information based on curves retrieved from field model look-up table built in sensor calibration. A multiple-field superimposition and a geometry based optimization are designed to find droplet location which guarantees both high accuracy and throughput. As the detection area is very small, the working distance between is about 5mm. So the light beam field can be regarded as a cylinder distribution in such distance levels. With this assumption, we use the least square method [45] to fit the two branch curves which are obtained from the previous model indexing step:

$$\{k, b\} = \arg \min_{k,b} \|Y - C\|_2 \quad s.t. \quad C(X) = kX + b. \quad (6)$$

After fitting, six analytical lines will be obtained. The droplet location is where the three peaks that match responding sensor model. This point can be identified by finding out all the crossing points of three lines with each from one sensor model. In practice, some deviation is inevitable due to the environment and hardware design variations. Therefore, we apply the center of the circumcircle of the triangle that is formed by three intersections to estimate the droplet location. If there are multiple circumcircles, the circle

---

Algorithm 1 Droplet Location Fine-tuning Algorithm

Input: D^1, D^2, D^3:Three set of time serial data obtained from the sensor out signal
$\quad\quad T_1(x, y), T_2(x, y), T_3(x, y)$:Trough value surface of each of the three pair of sensors
Output: (x^*, y^*):The x and y coordinate of the dropping location
1: pk_i =PeakDetection(D^i),$i = 1, 2, 3$
2: (l_{ia}, l_{ib}) = Intersection $\{pk_i \cap T_i(x, y), i = 1, 2, 3\}$
3: $A = \{(l_\alpha, l_\beta, l_\gamma)|\alpha \in \{1a, 1b\}, \beta \in \{2a, 2b\}, \gamma \in \{3a, 3b\}\}$
4: Set Circle $S = \emptyset$
5: **for** $(l_\alpha, l_\beta, l_\gamma) \in A$ **do**
6: $\quad\quad p_1 = l_\alpha \cap l_\beta, p_2 = l_\alpha \cap l_\gamma, p_3 = l_\beta \cap l_\gamma$
7: $\quad\quad$ Calculate Circle O from p_1, p_2, p_3
8: $\quad\quad S = S \cup O$
9: **end for**
10: $(x^*, y^*) = \arg \min_{(x,y)} r$ s.t. $O(r, x, y) \in S$

---

with the smallest radius will be taken as the final result. The whole algorithm can be implemented by the details in Algorithm 1.

During the detection process, a set of time serial data obtained from each sensor noted as D^i. Then the peak value detection will be applied on the flip over signal, where the peak value will represent the trough of the original data set. Then this peak value pk_i will be used to calculate the intersection of the beam model $T_i(x, y)$ and a plane where it is equal to pk_i, after the least square fitting it will generate two lines from each sensor pair.

We traverse all possible combinations of one line from each sensor which form the set A. In order to quantify the aggregation of the intersection of lines, we examine the radius of the circumcircle of the triangle formed by three lines. For each combination, the three lines' crossing points are noted by p_1, p_2 and p_3. Its circumcircle with radius r and center point coordinate (x, y) can be calculated and noted by $O(r, x, y)$.

The final step is to find out the circumcircle that has the minimum radius and its center point (x^*, y^*) will be the final droplet location result.

7 EVALUATION PLAN

In this section, we introduce our evaluation plan, which includes both simulation study and real-world experiment. However, our simulation and real-world strategies serve a different role from the traditional evaluation. *They are complementary to each other and evaluated by the different metrics.* But, in the conventional analysis, simulated study and real-world experiments are both evaluated by the same performance metric. Specifically, simulated study always serves as a demonstration of the proposed solution from theory perspective under the ideal environmental conditions, while the real-world study considers more practical parameters, whose model may vary a little from the one in the simulated study, and also verifies the performance and insight in the proposed solution. Therefore, the relationship between our simulation study and real-world study is different from the traditional case.

In our experiments, we use the location accuracy of the mimicking droplet as evaluating metric in the simulated study and use the recognition rate of defect droplet as judging criterion in the
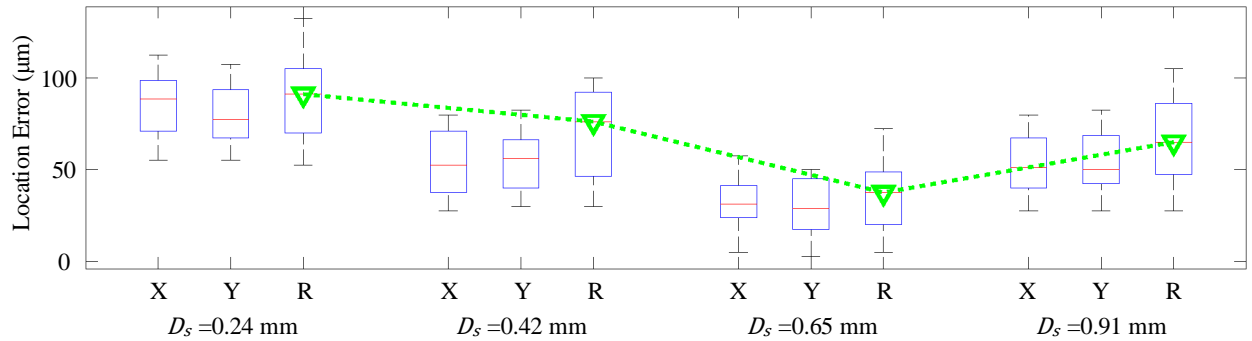
Figure 11: Overall accuracy results: X indicates the error in the horizontal direction, Y is the error in vertical direction and R is the error along the radial direction. The parameter D_s indicates the size of droplets.

real-world study. The reasons for our evaluation plan are as the followings:

- The droplet deposition is a complicated process, dynamic and uncertain, in the inkjet 3D printing. Many system parameters will affect the droplet behavior in the printing. What's worse, these parameters are even difficult to be quantitatively controlled. One representative example is the droplet size, which is a very tricky problem to always emit the same-size droplets using a current extruder. As our work is the first one to explore *in-situ* droplet micro-sensing solution for quality certification, we would like to focus on the most significant droplet location issue. Therefore, the simulation study is capable of examining the effectiveness of LuBan by placing a thin tip in the light beam field to mimic the same-size droplet with droplet location accuracy as the evaluation metric.
- As a quality assurance tool, the ultimate goal of our LuBan system is to improve the product reproducibility and process repeatability in practical inkjet 3D printing. Although some system parameters are too complicated to be accurately controlled, the real-world study is still a good method to examine the overall system performance improvement resulting from our LuBan system, including defect droplet detection rate and the whole system throughput. Therefore, the simulated study and real-world study are complementary to demonstrate the accuracy of our *in-situ* droplet micro-sensing system and the performance improvement of the entire inkjet 3D printing system.

In the following Section 8 and 9, we will elaborate the simulated study and real-world experiments, respectively. We will also analyze and discuss the evaluation results.

8 SIMULATED STUDY

We conduct extensive experiments to evaluate the performance of our droplet micro-sensing system, LuBan, towards precision 3D printing in this section. We first examine the overall accuracy of LuBan system. Then we characterize a typical spatial accuracy distribution in the light beam field. We also evaluate other sensitive environmental factors which may affect the precision, such as misalignment sensitivity.

8.1 Experimental Setup

In this simulated study, we use 950-nm infrared LED and photodiode sensor coming from a transmissive optical sensor with phototransistor output [3] to build the light beam field according to the three-pair sensor array layout. We use Arduino MEGA 2560 [42] to collect the data of sensors. Micro-controller of ATmega2560 with 16 MHz clock frequency, 16 channels of its 10-bit ADC are used for data acquisition of photodiode detector. We also adopt TI DM3730 [4] as the computing platform for integration-domain droplet location algorithm. It integrates a 1GHz ARM-Cortex A8 core [27] and 512 MByte on-board DDR SDRAM for computing intensive jobs.

For the droplet, we adopt a stainless tip to mimic its deposition process in light beam field due to the unpredictable droplet behavior in practical applications. This simulation can help comprehensively evaluate the performance of our LuBan system. We use horizontal and vertical stages controlled by step motors to move the relative position between the print head and the sensor array with a step of 0.05mm. We also provide four different sizes of stainless tips with the diameters as 0.24, 0.42, 0.65 and 0.91mm.

8.2 Overall Accuracy

In this experiment, we examine the accuracy of LuBan system to sense the position of the droplet. Considering the size of the droplet is a significant factor that varies over different applications of LuBan, we use all four types of stainless tips with a diameter as 0.24, 0.42, 0.65 and 0.91mm to mimic droplet size variability. We record the position of the stainless tip in advance and take this result as our ground truth. After the estimation of the location algorithm in LuBan, we collect the absolute error information from horizontal axis (X), vertical axis (Y) and radial axis (R). Note that the radial axis R indicates the Euclidean distance to the ideal position, i.e., $R = \sqrt{X^2 + Y^2}$. All the cases have 50 trials and our results are shown in Figure 11. We analyze Figure 11 from four aspects, high precision, optimal droplet size, X-Y similarity and high stability.

High Precision: We can observe that the overall accuracy of our LuBan system is about 100 microns, which sufficiently matches the sub-millimeter manufacturing accuracy of inkjet 3D printers [17, 33]. We take the median of the radial direction error as

our evaluation criterion. All the cases are under 100 microns, especially the 0.65mm case only with 42-micron error. Also, we can find that the errors decomposed into two axes are even smaller.

Optimal Droplet Size: When we compare the error information under different droplet sizes, we can find its trend is a typical single-valley curve, as the green dashed line with star marker shows in Figure 11. As the size of the droplet increases to 0.65mm, the error takes on a declining change. However, the error becomes larger as the size increases.

This optimum is because our location algorithm utilizes the interference of the beam field, if the droplet size is small, the interference will be too weak to be easily identified. If the droplet size is large, the interference is so strong that it covers over the variation of the beam field distribution. The location information will not be easily recovered. Therefore, we have an optimal droplet size option for a specific light beam field. What's more, if certain application constraints the droplet size, such as metal printing or bio-printing, we can also optimize the light beam field to achieve the optimal accuracy by configuring the droplet size.

X-Y Similarity: Specifically, we can observe that the error in the horizontal axis (X) has a similar trend with the vertical axis (Y). Their error distributions are similar in all four cases. The reason is that by deploying the sensor pairs in an axisymmetric way, it will increase the symmetry of the superimposed beam field distribution along X and Y directions. Thus their errors take on similar statistics under different droplet sizes. The radial error is a little larger than the other two sub-axis errors. In fact, the radial error is affected by both horizontal and vertical errors.

High Stability: If we have a closer look at the distance between the minimal and maximal errors of the radial direction, we can find that they have subtle variations in all four cases. This demonstrates our LuBan system has a good stability on droplet position sensing. Our location algorithm is based on analytical geometry and optimization technique, which enables the capability to resist obvious outliers. This property guarantees the stability of our LuBan sensing system. Without loss of generality, we choose droplet diameter of 0.65mm for the following simulated studies.

8.3 Spatial Accuracy Distribution

To make our accuracy distribution more concrete, we characterize the spatial accuracy distribution in the beam field superposition area which is also the sensor array working range. We move the stainless tip across the whole working range by the step of 0.05mm, monitored by our LuBan system. The characterization result is shown in Figure 12.

We can find that the spatial accuracy has smaller errors in the center area and around boundary area. Larger errors appear in the area between them. By carefully examining the fitting process of the *Gaussian* curve and the intersection line, more data points deviate in this area in both cases, which brings most of the detection error. More fundamentally, this is caused by the imperfect light beam field shape distribution which is not an exact cylinder. But this cylinder approximation can work well in a small range area. Additionally, by customizing the emitting infrared diode, especially the shape of the epoxy lens/case and the relative location of the P-N junction, better cylindrical light beam field can be obtained.
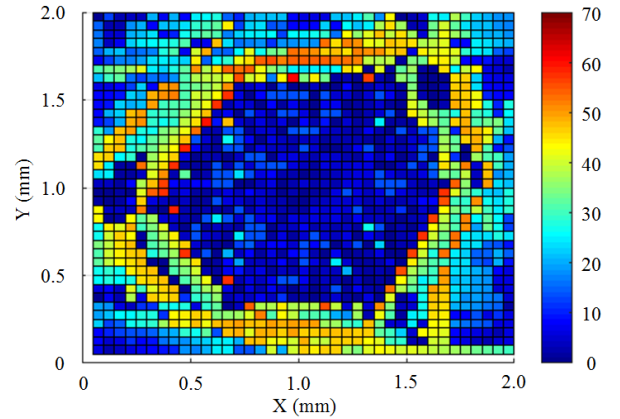

Figure 12: Spatial accuracy results of LuBan system.

This will greatly improve the detection accuracy. We also find that the entire distribution is a symmetrical pattern. This results from our symmetric layout of three diode pairs. This kind of error distribution is suitable for the droplet location detection, because in most cases, the droplet falls in the center area where higher accuracy is guaranteed.

8.4 Misalignment Sensitivity

The Luban system needs multiple sensor pairs to construct the symmetrical sensor layout. However, absolute symmetry is difficult to be guaranteed in practical applications. We aim to examine the sensor pair misalignment effect on LuBan system in this experiment. We intentionally misalign the sensor pairs by purpose of manual at five levels, -10 (counter-clockwise), -5, 0, 5, and 10 degrees, which are likely to appear in practice. We collect the error information under each testing case. Final results are shown in Figure 13.
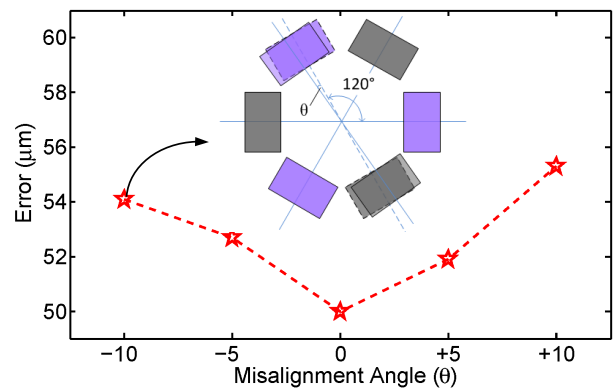

Figure 13: Accuracy under five misalignment cases. An example is provided to illustrate the misalignment.

From Figure 13, we can find that the small-angle misalignment does not cause much accuracy degradation. Although misaligned by 10 degrees, the accuracy is only decreased by about 4 microns.

This is because, in the calibration procedure, the information of each pair direction has been integrated into the beam field model. However, if the misalignment is too large, the emitted infrared beam field may be detected by not only the paired one with it but also the detector adjacent to it. This will violate our modeling assumption and bring large errors. So the sensor pair holds 120-degree angle with another pair in our preferred sensor layout. A misalignment within 10 degrees will be easily corrected in such layout. Therefore, our LuBan system can resist to the sensor pair misalignment in practical applications.

9 REAL-WORLD STUDY

In this section, we conduct the real-world study of applying our LuBan system to real inkjet 3D printing jobs. Specifically, we introduce our experimental setup. We also examine the defect droplet detection accuracy of our LuBan system in real applications. Finally, we investigate the sensing delay of LuBan and the system robustness to the ambient light noise.
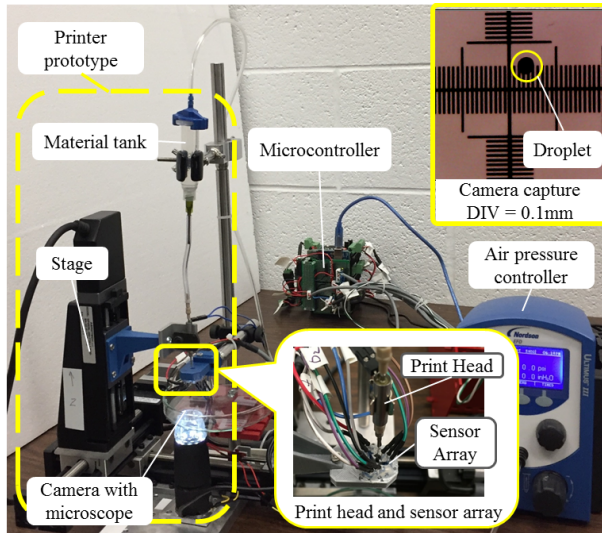

Figure 14: Prototype of our LuBan system, including 3D printer, sensor array, print head and control board.

9.1 Experimental Setup

We conduct real inkjet 3D printing on a prototype printer as shown in Figure 14. The printer prototype consists of a printing head, a material tank and an air pressure subsystem. The printing head has a micro-solenoid. When a voltage is applied, the valve is open and allows the liquid to flow out. By applying a short pulse voltage and air pressure over the material, a droplet can be generated at the orifice of the nozzle. Material tank stores the liquid material and the controlled air pressure is applied to control the droplet behavior. We examine four types of liquid materials, i.e., pure water, green ink (bio-ink), red ink (bio-ink) and black ink (bio-ink), where the colorful inks are commonly-used in bio-printing [20]. Each ink will mix with the water by volume percentage of 10%, 20% and 30%. We also provide two types of the nozzle, 0.13mm and 0.25mm, for

droplet size variation. For the ground truth, we use a camera with a microscope to examine the droplet position on the solidified part of the 3D printer.

9.2 Test Accuracy

We investigate the defect droplet accuracy of LuBan under three sensitive system parameters, i.e., droplet size, material and density. Different from the simulated study, the material of droplet becomes a significant factor to affect the precision of LuBan system. In the previous study, we use a stainless tip as a droplet simulator. We can simulate droplet size by tip diameter, but we can't simulate the material variations. In practical applications, it is very helpful to change the printing materials to fulfill different application requirements. As it is difficult to accurately control the size of the droplet, we identify droplet size by nozzle diameter, 0.13mm (0.005") and 0.25mm (0.01"). We also use three types of ink, red, green and black, to make droplets with different materials and percentage. We choose percentage as 10%, 20% and 30% ink mixing with water. In inkjet printing, the 100-micron deviation is allowed to guarantee the part printing quality [10]. Eventually, we collect the recognition rate of the defective droplet whose deviation is larger than 100 micron as our evaluation criterion. The detailed results are illustrated in Figure 15. We analyze Figure 15 from three aspects, high precision, material impact and concentration impact, as the followings:

High Precision: We can find that our LuBan has an extremely high recognition rate, more than 97%. Specifically, we first check the droplet size effect on accuracy. This part is consistent with the results from the simulated study. The large-size droplet can obtain better accuracy. Thus, it can achieve better recognition rate. We can even find that the larger-size droplet with 30% black ink can even achieve an accuracy of 99.68%.

Material Impact: We continue to investigate the material impact on recognition rate of defective droplets. As shown in Figure 15, the black ink is better than green ink, and the green ink is better than red ink. This is because the main interference effect on the beam field made by the droplet is absorption. Particles in the black ink can absorb the widest range of light in different wavelengths. Thus, it causes the largest light beam field disturbance. For green color, it is good at absorbing some lights. Thus it can improve the accuracy but not as good as the black color.

Concentration Impact: Finally, we check the concentration impact. We can observe that higher concentration can always obtain better accuracy. This is because of more particles in the water that can absorb more light energy. This will make more obvious interference in the light beam field. Therefore, this demonstrates the content of the liquid printing material can largely affect the defective droplet detection accuracy.

9.3 Delay Overhead Analysis

System Delay Characterization: In this section, we investigate the time efficiency of our LuBan system. We choose the green ink with a density of 20% as the droplet source in this experiment. We collect the runtime information of all the components in LuBan system, including sensor response of transforming light energy
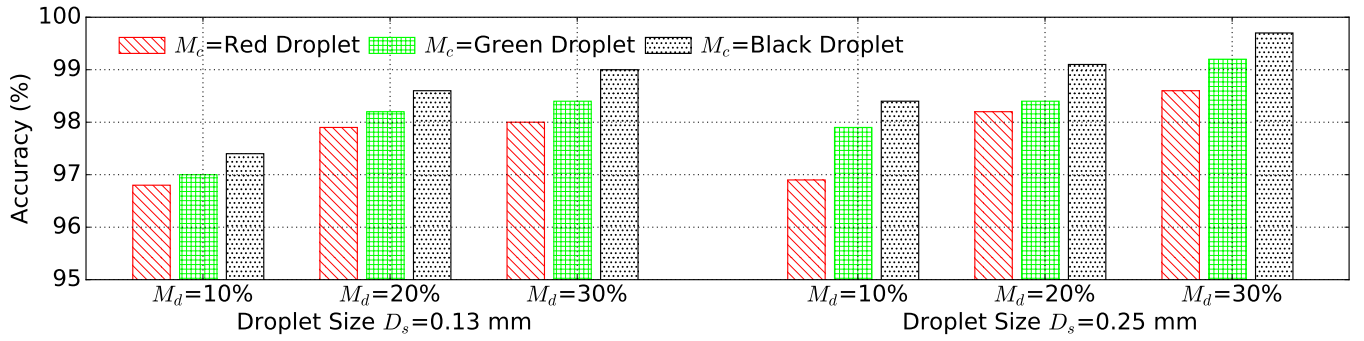
Figure 15: Accuracy of real world study. It compares the effect of droplet size (D_s), material color(M_c) and density (M_d).

into electric energy, analog-to-digital conversion and droplet location algorithm. The system-level runtime breakdown statistics are shown in Table 1.

Table 1: Runtime of all components in LuBan micro-sensing system.

Sensor Response	AD Conversion	Location Algorithm	Total Delay
10.6 μs	66.7 μs	1302.5 μs	1379.8 μs

From Table 1, we can find that the total delay of our LuBan system is about 1.38 ms. This is rapid enough to implement an *in-situ* correction to remove the defective droplets in inkjet 3D printing with a 5ms time bound [36]. Another observation is that droplet location algorithm takes up the majority of runtime by 94.4%. This is because the energy format transforming and ADC are both hardware-level operations. However, an integration-domain droplet location algorithm is implemented at the software level.

Algorithm Runtime Breakdown: We also would like to further analyze the time breakdown of droplet location algorithm. We use Gem5 [7] to simulate the ARM Cortex A8 core to collect the statistics of the runtime of each module in the droplet location algorithm. We also count the runtime from IO and memory since our algorithm is running on ARM core. The detailed runtime breakdown information is shown in Figure 16.

We can observe that the computing of droplet location algorithm is the bottleneck with 78.2% proportion, compared with the total 21.8% from both memory and IO. Inside the computing part, the geometry optimization is the main consumer, taking up 53.6% of the algorithm runtime. This optimization needs super computations on the ARM core while peak detection and model indexing execute simple arithmetic operations. This phenomenon provides us a direction to optimize the geometry optimization to further improve the sensing throughput of LuBan.

9.4 Robustness to Ambient Light Noise

Ambient light noise is always a practical issue to the light beam based sensing, especially in the open scenarios. In this experiment, we investigate the light noise effect on our LuBan System. Our detector has an operation wavelength at 950nm, which is in the infrared range that can avoid some of the influence of visible light in daily
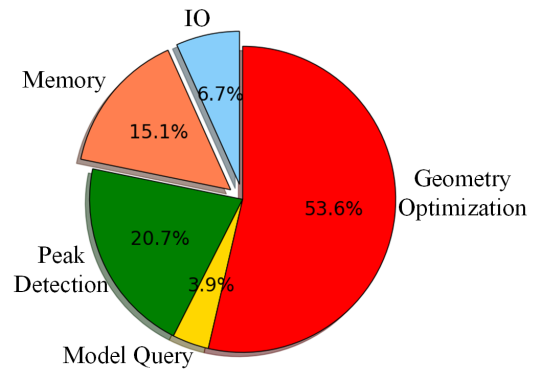

Figure 16: The runtime breakdown of the droplet location algorithm on the ARM platform.

life. We set different levels of visible light strength, 10 mW/cm^2, 50 mW/cm^2, 100 mW/cm^2 and 200 mW/cm^2, for the experiment environment. We repeat the experiment 10 times randomly for each noise level. Then we apply our location algorithm to estimate the position of the droplet. The detection accuracy of defect droplet is shown in Figure 17.
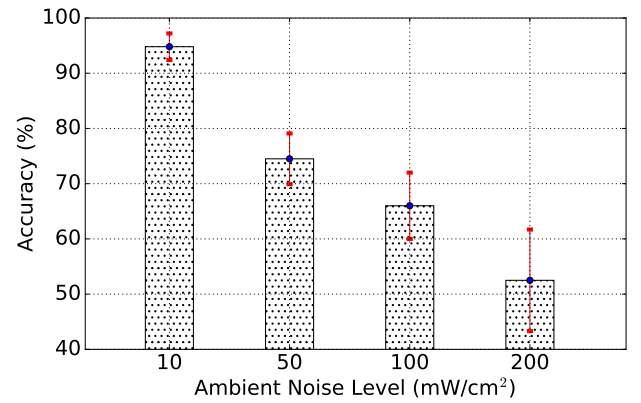

Figure 17: Accuracy of LuBan system under four environmental noise levels.

We can observe that LuBan can successfully cope with the noise no more than 10 mW/cm^2. But as noise level continues to increase, LuBan will compromise large accuracy. In fact, our location estimation algorithm is based on the combination of analytical geometry and optimization. Thus, it has a light-weight noise immune ability. However, as the noise increases to hide valid information, it will distort the fitting process of the Gaussian curve surfaces. The failure of fitting results compromises larger accuracy. Therefore, we should choose an environment with less light noise when using LuBan.

10 RELATED WORK

There is some research work related to our LuBan system design in the inkjet 3D printing application. We summarize them into two main categories:

3D Printer Monitoring: Monitoring for the 3D printer to ensure its normal working state is a hot topic. Faes et al. designed a process monitoring system for extrusion based 3D printing with a laser as its sensing tool [14]. However, this method is based on the off-line monitoring. It cannot be integrated with the *in-situ* quality assurance and certification system. Some other work [12, 41] focused their attention on the online temperature monitoring of 3D printer. They built a complete control loop to correct the exceptions in time. Different from the high precision requirement of our droplet monitoring application, these works were to optimize the time efficiency under a much looser accuracy constraint.

Light-based Sensing: Light is a promising approach in sensing technology for its property of stability and free-interference. Li et al. developed a practical human sensing modality in the light [23]. They could recognize the person posture with LED arrays and optimization method based on shadow information. This work cannot enable the sub-millimeter level application due to its shadow analysis from light. On the other hand, light-based droplet monitoring is investigated in the microfluidic community. These researches were almost concentrating on monitoring the size and velocity of the droplet to guarantee its usability for subsequent processing [25, 30]. But the droplet location precision was not well studied, which is the biggest concern in inkjet 3D printing quality assurance.

11 CONCLUSION AND FUTURE WORK

In this paper, we investigated a droplet micro-sensing system, LuBan, to examine the quality assurance of inkjet 3D printing. Our micro-sensing system was based on interference effect from light beam field to detect the defect droplet in the printing process. We started from the basics of inkjet 3D printer. We introduced the concept of light beam field and the promising field interference with droplets. For the practical challenges to design LuBan system, we presented specific strategies to tackle the problems. The integral sensing was applied to reduce the measurement complexity of the complicated interference pattern. We chose a three-pair emitter-detector solution to design the hardware prototype of sensing for LuBan. Moreover, we developed a geometry based optimization approach to accurately estimate the droplet position in the field space. Extensive experiments indicate that our LuBan can achieve sub-millimeter level precision, which can meet the quality assurance requirements. In the real-world printing study, LuBan can

detect more than 99% defective droplets to drastically improve the part quality of inkjet 3D printer.

In the future work, we consider handling the imperfection of the droplets, such as satellite effects and multiple droplets aggregation. On the other hand, we also plan to further improve the performance of droplet micro-sensing for inkjet 3D printer quality assurance applications.

REFERENCES

[1] [n. d.]. https://en.wikipedia.org/wiki/Lu_Ban/. ([n. d.]).
[2] [n. d.]. Planck constant. https://en.wikipedia.org/wiki/Planck_constant. ([n. d.]).
[3] Muhammad Taufiq Bin Zainul Abidin, Mohd Khairul Ridhwan Rosli, Sarah Addyani Shamsuddin, Nina Korlina Madzhi, and Mohd Firdaus Abdullah. 2013. Initial quantitative comparison of 940nm and 950nm infrared sensor performance for measuring glucose non-invasively. In *Smart Instrumentation, Measurement and Applications (ICSIMA), 2013 IEEE International Conference on.* IEEE, 1–6.
[4] PK Aby, Anumol Jose, Bibin Jose, LD Dinu, Jomon John, and G Sabarinath. 2011. Implementation and optimization of embedded face detection system. In *Signal Processing, Communication, Computing and Networking Technologies (ICSCCN), International Conference on.* IEEE, 250–253.
[5] Francesco Aieta, Patrice Genevet, Nanfang Yu, Mikhail A Kats, Zeno Gaburro, and Federico Capasso. 2012. Out-of-plane reflection and refraction of light by anisotropic optical antenna metasurfaces with phase discontinuities. *Nano letters* 12, 3 (2012), 1702–1706.
[6] Jerry Ajay, Chen Song, Aditya Singh Rathore, Chi Zhou, and Wenyao Xu. 2017. 3DGates: An Instruction-Level Energy Analysis and Optimization of 3D Printers. In *Proceedings of the Twenty-Second International Conference on Architectural Support for Programming Languages and Operating Systems.* ACM, 419–433.
[7] Nathan Binkert, Bradford Beckmann, Gabriel Black, Steven K Reinhardt, Ali Saidi, Arkaprava Basu, Joel Hestness, Derek R Hower, Tushar Krishna, Somayeh Sardashti, et al. 2011. The gem5 simulator. *ACM SIGARCH Computer Architecture News* 39, 2 (2011), 1–7.
[8] Gaetano Borriello, Alan Liu, Tony Offer, Christopher Palistrant, and Richard Sharp. 2005. Walrus: wireless acoustic location with room-level resolution using ultrasound. In *Proceedings of the 3rd international conference on Mobile systems, applications, and services.* ACM, 191–203.
[9] Susmita Bose, Sahar Vahabzadeh, and Amit Bandyopadhyay. 2013. Bone tissue engineering using 3D printing. *Materials Today* 16, 12 (2013), 496–504.
[10] Paul Calvert. 2001. Inkjet printing for materials and devices. *Chemistry of materials* 13, 10 (2001), 3299–3305.
[11] Brian Derby. 2010. Inkjet printing of functional and structural materials: fluid property requirements, feature stability, and resolution. *Annual Review of Materials Research* 40 (2010), 395–414.
[12] Ralph B Dinwiddie, Lonnie J Love, and John C Rowe. 2013. Real-time process monitoring and temperature mapping of a 3D polymer printing process. In *SPIE Defense, Security, and Sensing.* International Society for Optics and Photonics, 87050L–87050L.
[13] Nabil Eid, Yuko Ito, Kentaro Maemura, and Yoshinori Otsuki. 2013. Elevated autophagic sequestration of mitochondria and lipid droplets in steatotic hepatocytes of chronic ethanol-treated rats: an immunohistochemical and electron microscopic study. *Journal of molecular histology* 44, 3 (2013), 311–326.
[14] Matthias Faes, Wim Abbeloos, Frederik Vogeler, Hans Valkenaers, Kurt Coppens, Eleonora Ferraris, et al. 2014. Process monitoring of extrusion based 3D printing via laser scanning. In *PMI 2014 Conference Proceedings*, Vol. 6. 363–367.
[15] Luigi Maria Galantucci, Fulvio Lavecchia, and Gianluca Percoco. 2009. Experimental study aiming to enhance the surface finish of fused deposition modeled parts. *CIRP Annals-Manufacturing Technology* 58, 1 (2009), 189–192.
[16] Paul Green, Jan Kautz, Wojciech Matusik, and Frédo Durand. 2006. View-dependent precomputed light transport using nonlinear gaussian function approximations. In *Proceedings of the 2006 symposium on Interactive 3D graphics and games.* ACM, 7–14.
[17] Bethany C Gross, Jayda L Erkal, Sarah Y Lockwood, Chengpeng Chen, and Dana M Spence. 2014. Evaluation of 3D printing and its potential impact on biotechnology and the chemical sciences. *Analytical chemistry* 86, 7 (2014), 3240–3253.

[18] Chen Hongyang, Deng Ping, Xu Yongjun, and Li Xiaowei. 2005. A robust location algorithm with biased extended Kalman filtering of TDOA data for wireless sensor networks. In *Proceedings. 2005 International Conference on Wireless Communications, Networking and Mobile Computing, 2005.*, Vol. 2. IEEE, 883–886.

[19] Seung Hwan Ko, Jaewon Chung, Nico Hotz, Koo Hyun Nam, and Costas P Grigoropoulos. 2010. Metal nanoparticle direct inkjet printing for low-temperature 3D micro metal structure fabrication. *Journal of Micromechanics and Microengineering* 20, 12 (2010), 125010.

[20] David B Kolesky, Ryan L Truby, A Gladman, Travis A Busbee, Kimberly A Homan, and Jennifer A Lewis. 2014. 3D bioprinting of vascularized, heterogeneous cell-laden tissue constructs. *Advanced materials* 26, 19 (2014), 3124–3130.

[21] Yves Lacouture and Denis Cousineau. 2008. How to use MATLAB to fit the ex-Gaussian and other probability functions to a distribution of response times. *Tutorials in Quantitative Methods for Psychology* 4, 1 (2008), 35–45.

[22] Hsien-Hsueh Lee, Kan-Sen Chou, and Kuo-Cheng Huang. 2005. Inkjet printing of nanosized silver colloids. *Nanotechnology* 16, 10 (2005), 2436.

[23] Tianxing Li, Qiang Liu, and Xia Zhou. 2016. Practical Human Sensing in the Light. In *Proceedings of the 14th Annual International Conference on Mobile Systems, Applications, and Services.* ACM.

[24] Yiyan Li, Hongzhong Li, and R Jacob Baker. 2015. A low-cost and high-resolution droplet position detector for an intelligent electrowetting on dielectric device. *Journal of laboratory automation* 20, 6 (2015), 663–669.

[25] Martin Löffler-Mang and Jürg Joss. 2000. An optical disdrometer for measuring size and velocity of hydrometeors. *Journal of Atmospheric and Oceanic Technology* 17, 2 (2000), 130–139.

[26] Georgios Mastorakis and Dimitrios Makris. 2014. Fall detection system using KinectéĽ̌ĕ̌æĺŽ infrared sensor. *Journal of Real-Time Image Processing* 9, 4 (2014), 635–646.

[27] Teresa L McLaurin. 2006. The Challenge of Testing the ARM CORTEX-A8/sup TM/Microprocessor Core. In *Test Conference, 2006. ITC'06. IEEE International.* IEEE, 1–10.

[28] Eduardo Napadensky. 2010. Inkjet 3D printing. *The Chemistry of Inkjet Inks. New Jersey-London-Singapore: World Scientific* (2010), 255–67.

[29] Lionel M Ni, Yunhao Liu, Yiu Cho Lau, and Abhishek P Patil. 2004. LANDMARC: indoor location sensing using active RFID. *Wireless networks* 10, 6 (2004), 701–710.

[30] Xize Niu, Mengying Zhang, Suili Peng, Weijia Wen, and Ping Sheng. 2007. Real-time detection, control, and sorting of microfluidic droplets. *Biomicrofluidics* 1, 4 (2007), 044101.

[31] Kyung-Wook Paik, Jin-Gul Hyun, Sangyong Lee, and Kyung-Woon Jang. 2006. Epoxy/BaTiO3 (SrTiO3) composite films and pastes for high dielectric constant and low tolerance embedded capacitors in organic substrates. In *2006 1st Electronic Systemintegration Technology Conference*, Vol. 2. IEEE, 794–801.

[32] Jeong Park, Moowhan Shin, and Chin C Lee. 2004. Measurement of temperature profiles on visible light-emitting diodes by use of a nematic liquid crystal and an infrared laser. *Optics letters* 29, 22 (2004), 2656–2658.

[33] Kris Pataky, Thomas Braschler, Andrea Negro, Philippe Renaud, Matthias P Lutolf, and Juergen Brugger. 2012. Microdrop Printing of Hydrogel Bioinks into 3D Tissue-Like Geometries. *Advanced Materials* 24, 3 (2012), 391–396.

[34] B Subba Rao, B Shalini, B Krishna Teja, and B Kalpana. 2013. Infrared diode laser retinal treatment for chronic headache. *Journal of Evolution of Medical and Dental Sciences* 2, 50 (2013), 9722–9726.

[35] Francisco J Rodríguez-Fortuño, Giuseppe Marino, Pavel Ginzburg, Daniel OéŰşãČçonnor, Alejandro Martínez, Gregory A Wurtz, and Anatoly V Zayats. 2013. Near-field interference for the unidirectional excitation of electromagnetic guided modes. *Science* 340, 6130 (2013), 328–330.

[36] Rachel E Saunders, Julie E Gough, and Brian Derby. 2008. Delivery of human fibroblast cells by piezoelectric drop-on-demand inkjet printing. *Biomaterials* 29, 2 (2008), 193–203.

[37] Felix Scholkmann, Jens Boss, and Martin Wolf. 2012. An efficient algorithm for automatic peak detection in noisy periodic and quasi-periodic signals. *Algorithms* 5, 4 (2012), 588–603.

[38] Daniela Nascimento Silva, Marilia Gerhardt De Oliveira, Eduardo Meurer, Maria Inês Meurer, Jorge Vicente Lopes da Silva, and Ailton Santa-Bárbara. 2008. Dimensional error in selective laser sintering and 3D-printing of models for craniomaxillary anatomy reconstruction. *Journal of cranio-maxillofacial surgery* 36, 8 (2008), 443–449.

[39] Justyna Skowyra, Katarzyna Pietrzak, and Mohamed A Alhnan. 2015. Fabrication of extended-release patient-tailored prednisolone tablets via fused deposition modelling (FDM) 3D printing. *European Journal of Pharmaceutical Sciences* 68 (2015), 11–17.

[40] Chen Song, Feng Lin, Zhongjie Ba, Kui Ren, Chi Zhou, and Wenyao Xu. 2016. My smartphone knows what you print: Exploring smartphone-based side-channel attacks against 3d printers. In *Proceedings of the 2016 ACM SIGSAC Conference on Computer and Communications Security.* ACM, 895–907.

[41] Lijun Song and Jyoti Mazumder. 2011. Feedback control of melt pool temperature during laser cladding process. *IEEE Transactions on Control Systems Technology* 19, 6 (2011), 1349–1356.

[42] Imam Tazi, Kuwat Triyana, and Dwi Siswanta. 2016. A novel Arduino Mega 2560 microcontroller-based electronic tongue for dairy product classification. In *ADVANCES OF SCIENCE AND TECHNOLOGY FOR SOCIETY: Proceedings of the 1st International Conference on Science and Technology 2015 (ICST-2015)*, Vol. 1755. AIP Publishing, 170003.

[43] Łukasz Tymecki and Robert Koncki. 2009. Simplified paired-emitter–detector-diodes-based photometry with improved sensitivity. *Analytica chimica acta* 639, 1 (2009), 73–77.

[44] Łukasz Tymecki, Marta Pokrzywnicka, and Robert Koncki. 2008. Paired emitter detector diode (PEDD)-based photometry–an alternative approach. *Analyst* 133, 11 (2008), 1501–1504.

[45] Sabine Van Huffel and Philippe Lemmerling. 2013. *Total least squares and errors-in-variables modeling: Analysis, algorithms and applications.* Springer Science & Business Media.

[46] Elke M Vinck, Barbara J Cagnie, Maria J Cornelissen, Heidi A Declercq, and Dirk C Cambier. 2003. Increased fibroblast proliferation induced by light emitting diode and low power laser irradiation. *Lasers in medical science* 18, 2 (2003), 95–99.

[47] Jie Wang, Alvaro Goyanes, Simon Gaisford, and Abdul W Basit. 2016. Stereolithographic (SLA) 3D printing of oral modified-release dosage forms. *International journal of pharmaceutics* 503, 1 (2016), 207–212.

[48] Lucas P Watkins and Haw Yang. 2005. Detection of intensity change points in time-resolved single-molecule measurements. *The Journal of Physical Chemistry B* 109, 1 (2005), 617–628.